

Non-standard bone simulations: Verification and validation

Martin Ruess · David Tal · Nir Trabelsi · Zohar Yosibash · Ernst Rank

Received: date / Accepted: date

Abstract Standard methods for predicting bone's mechanical response from quantitative computer-tomography (qCT) scans are mainly based on classical h-version Finite Element Methods (FEMs). This approach is often limited in terms of numerical accuracy and efficiency due to the low order polynomial approximation model, the need for segmentation, and the use of piecewise constant material properties assignment. Herein a non-standard method, the Finite Cell Method (FCM), is proposed for predicting the mechanical response of the human femur. The FCM is free of the above limitations associated with h-FEMs and is orders of magnitude more efficient, allowing its use in the setting of computational steering. This non-standard method applies a fictitious domain approach to simplify the modeling of a complex bone geometry obtained directly from

a qCT scan, and takes into consideration easily the heterogeneous material distribution of the various bone regions of the femur.

The fundamental principles and properties of the FCM are briefly described in relation to bone analysis, providing a theoretical basis for the comparison with the p-FEM as a reference analysis and simulation method of high quality. Both, p-FEM and FCM results are validated by comparison to an in-vitro experiment on a fresh-frozen femur.

Keywords High-Order FEM · Fictitious Domain Method · Bone Mechanics · Human Femur

1 Introduction

Patient-specific prediction and monitoring of in-vivo bone strength is a key aspect in clinical routine to decide on the need for surgical intervention of e.g. osteoporotic bone. 2D X-ray images in various positions and 3D models from computer tomography scans are the traditional information basis for such lasting decisions, providing the bone geometry and structural information derived from the apparent bone density distribution. Technological developments enable models of today to be enriched by patient-specific biomechanical properties. Information about the elastic response of e.g. a loaded human femur in terms of strains and stresses provide a more complete comprehension of its true stability and strength.

The Finite Element Method (FEM) has become the standard approach for patient-specific

Martin Ruess · Ernst Rank
Chair for Computation in Engineering, Technische Universität München, Munich, Germany
Tel.: +49-89-289-22425/-23047
Fax: +49-89-289-25051
E-mail: ruess@tum.de / rank@bv.tum.de

David Tal · Nir Trabelsi
Department of Mechanical Engineering, Ben-Gurion-University of the Negev, Beer Sheva, Israel
Tel: +972-8-647-7025
E-mail: nirtr@bgu.ac.il / tda@bgu.ac.il

Zohar Yosibash
Department of Mechanical Engineering, Ben-Gurion-University of the Negev, Beer Sheva, Israel
Tel: +972-8-647-7103
E-mail: zohary@bgu.ac.il
(Research performed while on Sabbatical leave at the Chair for Computation in Engineering at the Technische Universität München)

bone analysis on the basis of qCT-scans. Besides the large number of publications in this field, based on the conventional h-version of the FEM (h-FEMs) [1–5], other more sophisticated numerical analysis schemes for the prediction of strains and stresses of high numerical accuracy have gained more attention over the last years. Yosibash et al. [6,7] proposed the application of the p-version of the FEM (p-FEMs) for a smoothed heterogeneous material distribution. The method allows simple p-refinement on a fixed mesh which well describes bone’s geometry, until numerical convergence is reached allowing for verification of the quality of the numerical approximation. Comparisons performed between the verified p-FE results and in-vitro experiments on three fresh-frozen human femurs provided evidence on the validity of these methods. Taddei et al. [8] applied a meshless method labeled the Meshless Cell Method (MCM), for subject-specific strain prediction. Their method was particularly developed for the elasticity analysis of CT-scanned bone models. They document results of an ongoing research including a comparison of strains and displacements obtained by their method and by a standard FEM implementation with experimental results. A correlation analysis of their results show acceptable values for the MCM ($R^2 = 0.85^1$) with a tendency to overestimate the strains. It is important to note that this method is completely different from the *Finite Cell Method* that is addressed in the course of this contribution.

In this paper we introduce a non-standard simulation method for the elasticity analysis of a human femur. The FCM is a fictitious domain approach that exploits the higher order Ansatz space of the p-FEM. The nature of fictitious domain methods widely prevents from tedious and often not foolproof and unique meshing of geometrically complex domains such as the human femur. This property simplifies the modelling process dramatically but shifts the modelling effort to the numerical solution method that has to capture the true structural model. A recent mechanical experiment on a fresh-frozen human femur, named FF4, is described which serves as the basis for validating the numerical results. The experimental setup is simulated with the verified and validated p-FEM developed in the group of Yosibash [6,7,9]. With sev-

eral tested bones and bone models the p-FEM was shown to be robust and accurate and has therefore been chosen as a reference solution to the newly developed FCM [10,11]. Herein, we provide a comparison of the complete analysis approach of the two methods to reveal their pros and cons and to particularly demonstrate that the FCM can compete with established methods for a reliable and accurate analysis result. Due to its high efficiency, the FCM enables computational steering and visualization - a topic covered by [12].

The paper is organized as follows: In section 2 we report on the experiments with a fresh-frozen human femur used for validation of the numerical simulations. Section 3 introduces the two applied analysis schemes, the p-FEM and the FCM. In subsection 3.1 the p-FEM is briefly described with emphasis on bone geometry determination and material properties assignment. Thereafter subsection 3.2 covers the FCM approach and the particular alterations towards its application for bone analysis. The integration scheme on cell level and the application of weakly enforced boundary conditions on the basis of a Nitsche formulation are addressed and discussed. The ensuing subsection verifies the accuracy of the FCM in comparison to the p-FEM, addressing a benchmark problem with heterogeneous material distribution to demonstrate the quality of the applied integration schemes. This section also introduces the qCT-derived voxel model of the human femur. In section 4 the numerical results for both the FCM and p-FEM are compared to the in-vitro experimental observations. Finally we summarize and discuss our results in section 5.

2 An in-vitro experiment on a fresh-frozen human femur

The in-vitro experiment described in the following serves as a basis for the numerical modelling procedure of the two proposed simulation methods introduced in section 3 and is therefore presented first.

A fresh frozen femur of a 63 years old male donor (denoted as FF4) was defrosted, cleaned from soft tissues and cut to a total length of 323mm . It was positioned vertically in a 100mm deep steel cylinder (a total of 223mm bone is tested) and secured to prevent

¹ R: coefficient of linear regression

movement by PMMA. The femur, along with five K_2HPO_4 calibration phantom burettes were immersed in a basin and qCT scanned by a clinical Phillips Brilliance 64 CT (Eindhoven, Netherlands): $120kVp$, $250mAs$, 1.25 slice thickness, axial scan without overlap, and pixel size of $0.195mm$ (the bone shaft was tilted by 5.5° in respect to the z direction of the CT scan).

Following the CT scan, it was loaded in a compression Zwick-1445 testing machine. Prior to loading, thirteen uniaxial strain gauges were bonded on bone's surface: seven at the proximal femur neck area (denoted SGs 1,2,7,8,11,12,13), three in the vicinity of the greater and lesser trochanter (denoted SGs 3,4,9), and three on the bone medial and lateral shaft areas (denoted SGs 5,6,10) (see Figure 1). The precise location of the SGs was determined by another CT-scan of the femur after the SGs were bonded. Two linear displacement sensors (LDS) were used to measure the vertical and horizontal head displacements at the lower part of the head and most horizontal part of it.

After loading the femur by a $100N$ pre-load, forces of $500N$ and $1000N$ were applied along the axis of the femur shaft using different loading connectors (either a flat surface or by a conical surface) and at different loading rates ($1/60$, $1/6$ and $1 mm/s$). Each loading scenario was repeated three or four times to confirm repeatability.

During all tests and load rates a linear strain-load and displacement-load relation was obtained, almost independent of the load rate. The displacements and strains measured during the experiment are used for comparison with those extracted from the p-FEM and FCM models.

Three out of the 13 SGs (SG8, SG11 and SG13) yielded unreasonable readings (probably due to measurements or installation problems) thus are discarded in the comparison process. A summary of the experimental measurements including the two displacements (vertical and horizontal) and the thirteen strains is provided in the last column of Table 3 (section 4).

3 Bone model generation from CT scans, material properties and boundary conditions

In this chapter we describe the p-FEM, the FCM and the specific model generation for the elasticity analysis of a human femur to predict displacements and the strain distribution on the bone surface.

3.1 Patient-Specific p-FEMs for femurs

As a mean for comparison to the FCM method, the p-FEM, shown to provide results of high accuracy and efficiency in [6,9], is applied for the analysis of the same FF4 femur. The p-FE model generation is based on qCT scans of a patient-specific femur and has already been described in the aforementioned publications, thus we provide herein only a short overview. A geometrical 3-D model of the femur is created by firstly identifying in each qCT slice the outer boundary of the bone and the cortical/trabecular interface, thereafter smoothing these boundaries and creating a point-cloud which is imported into a CAD system enabling the generation of a 3-D solid (an in-house segmentation code is used for this purpose). The solid model is imported into a p-FE code and automatically meshed by tetrahedral elements. The blending function method is used to map elements to the standard element enabling an accurate representation of the bone surfaces. The entire semi-automatic process is schematically illustrated in Figure 2 and is accomplished in a time-frame of about an hour.

Material properties assignment The qCT-scan of the bone results in a DICOM (Digital Imaging and Communications in Medicine) format that essentially provides the distribution of the radiodensity of the scanned subject in terms of Hounsfield Units (HU), the resolution for each slice of the scan, including layer and pixel spacing for a unique geometry description. In addition to the bone, a calibration phantom device was included (see section 2) for a linear conversion between HUs and an equivalent mineral density $\rho_{eqm}[g/cm^3]$ that is used as basis value for the derivation of the pointwise material properties for the p-FEM and FCM, and to distinguish whether the points are associated with the cortical or the trabecular regions. The

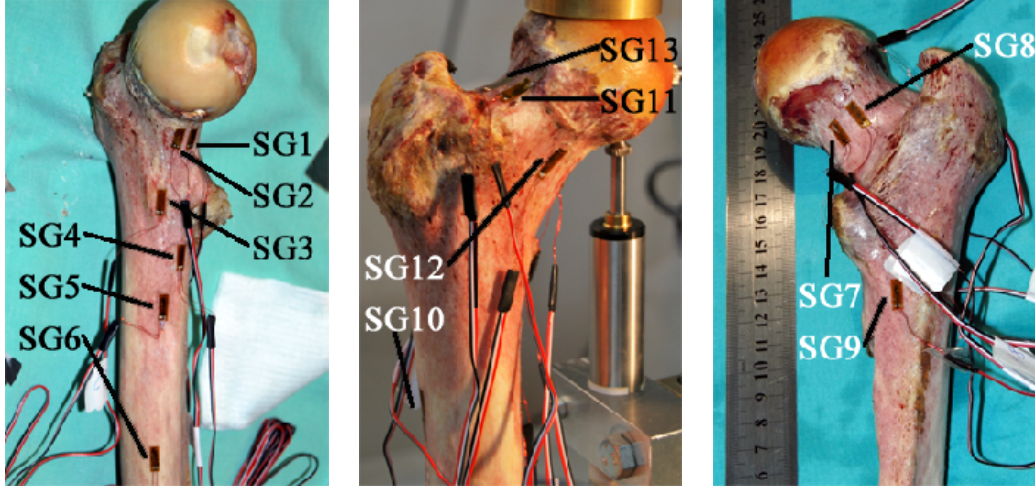


Fig. 1 Strain gauge locations on the fresh frozen femur of a 63 year old donor – denoted by FF4.

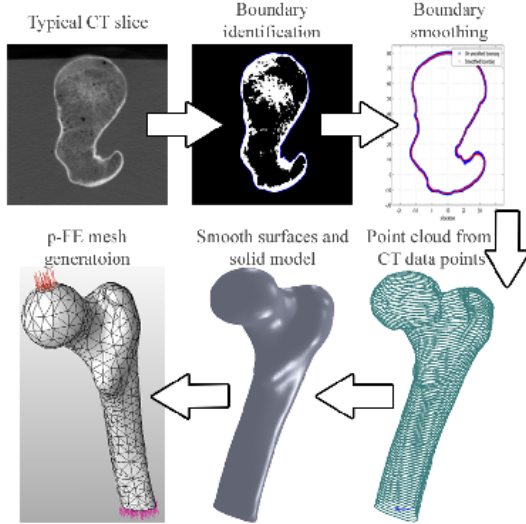


Fig. 2 The different stages in creating a p-FE model from the qCT scans.

following relation was found:

$$\rho_{eqm} = 10^{-3}(0.793) \times HU \quad (1)$$

Inhomogeneous, location dependent Young modulus, shown to well represent experimental observations in [6,7,9], based on [13] are assigned:

$$\rho_{ash} = 0.001 \times (1.22 \rho_{eqm} + 0.0523) [g/cm^3] \quad (2)$$

$$E_{cort} = 10200 \times \rho_{ash}^{2.01} [MPa] \quad (3)$$

$$E_{trab} = 5307 \times \rho_{ash} + 469 [MPa] \quad (4)$$

with a fixed Poisson ratio $\nu = 0.3$.

Boundary conditions With respect to the femur presented in section 2, the p-FE model was clamped at the distal part of the femur shaft whereas the head is loaded with a force of $1000N$ at a 5.5° angle so to be aligned with the femur shaft axis as in the experimental setting. This force is applied as traction on a flat face at the top of the femur head. An illustration of the FE model and the corresponding experiment is shown in Figure 3. Verification was performed

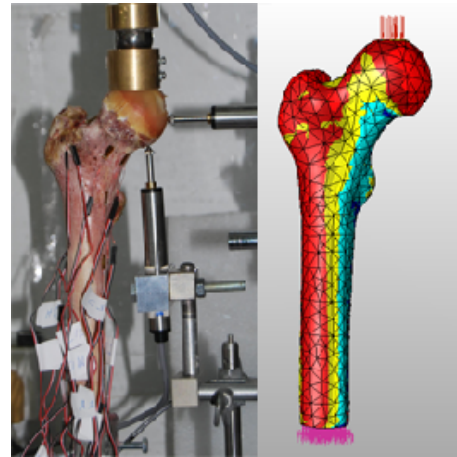


Fig. 3 FF4 experiment and principal strains on the surface of the p-FE mesh.

by increasing the polynomial degree in the p-FE analysis examining convergence in the data of interest (see Table 1 and Figures 11,12).

Table 1 FF4 p-FE verification (3522 tetrahedral elements)

p level	DOF	% Rel. error in energy norm	% Rel. error in U_z
1	2874	78.94	-
2	18342	14.58	65.88
3	56973	12.46	0.50
4	129333	11.86	0.14
5	245988	11.52	0.07
6	417504	11.26	0.05

3.2 Patient-Specific Finite Cell Method for the femur

The FCM as proposed in [10] is a fictitious domain method that exploits hierarchic Legendre-based Ansatz spaces as classically applied in p-FEMs, thus keeping essential properties with regard to the convergence behavior and error estimation. The method appears to be well-suited for complex geometries of the physical domain and multi-material interfaces as they are apparent for voxel-based bone mechanics.

The basic idea of the method is summarized in compact form in the following. A more detailed description is provided in [10,11].

3.2.1 The Finite Cell Method - Governing integral equations

Based on the principle of virtual displacements, the FCM satisfies the governing integral equations within a simplified domain of computation. The method embeds the physical domain of interest Ω in an extended cell domain Ω_C that is generated on a Cartesian grid. The governing integral equations are evaluated on the physical domain Ω by a refined numerical integration scheme that captures the true boundary $\partial\Omega$ (Fig. 4). The domain extension on a Cartesian grid essentially simplifies the modelling of complex geometries or geometries with multi-material interfaces and is one of the basic principles of the FCM but is not necessarily a restriction of the fictitious domain approach. A more general extension domain including distorted cells is also applicable and is partly used in the following analysis model to simplify the implementation of Neumann boundary conditions (Sec. 3.2.4).

In the context of a bone embedded in the CT scan frame, one may imagine the bone to be Ω whereas the entire CT frame by Ω_C .

In general, assume that Dirichlet boundary conditions are prescribed on a part of the physical domain's boundary and traction boundary conditions are prescribed on the other part the boundary:

$$\mathbf{u} = \mathbf{u}_0 \quad \text{on } \partial\Omega_u \quad (5)$$

$$\mathbf{t} = \mathbf{t}_0 \quad \text{on } \partial\Omega_t \quad (6)$$

where

$$\partial\Omega = \partial\Omega_u \cup \partial\Omega_t \quad \wedge \quad \partial\Omega_u \cap \partial\Omega_t = \emptyset$$

The principle of virtual displacements in the physical domain Ω is stated as:

$$\int_{\Omega} \delta \boldsymbol{\epsilon}^T \boldsymbol{\sigma} dv = \int_{\Omega} \delta \mathbf{u}^T \mathbf{p}_V dv + \int_{\partial\Omega_u} \delta \mathbf{u}^T \mathbf{t} da + \int_{\partial\Omega_t} \delta \mathbf{u}^T \mathbf{t}_0 da \quad (7)$$

$$\mathbf{x} \in \partial\Omega_u \Rightarrow \mathbf{u} = \mathbf{u}_0$$

with $\boldsymbol{\epsilon}$ and $\boldsymbol{\sigma}$ representing the strain and stress vectors in Voigt notation and \mathbf{u} the displacement vector. Equation (7) is an extension of the well-known principle of virtual displacements. It differs from the conventional principle in the unknown stress vector \mathbf{t} over the surface $\partial\Omega_u$ of prescribed displacements. The extended form is derived from a weighted residual formulation for the governing differential equations of the theory of elasticity (e.g. [14]) in preparation for the introduction of weakly satisfied boundary conditions (see section 3.2.4).

In the framework of linear elasticity Hooke's law reads: $\boldsymbol{\sigma}(\mathbf{x}) = [\mathbf{C}] \boldsymbol{\epsilon}(\mathbf{x})$ so that the stresses within the cell domain depend on α such that:

$$[\mathbf{C}_{\alpha}(\mathbf{x})] = \alpha [\mathbf{C}] \begin{cases} \alpha = 1 \quad \forall \mathbf{x} \in \Omega \\ \alpha = \epsilon \quad \forall \mathbf{x} \in \Omega_C \setminus \Omega \end{cases} \quad (8)$$

For points in Ω_C that are not contained in Ω , a Young's modulus is set to a small value $\hat{\epsilon}$ to represent the cell extension domain with material values equal to zero and to ensure a sufficient numerical stability of the formulation. A choice of $\hat{\epsilon}$ as $(\max(E) \cdot \epsilon^2)^{0.25}$ with $\max(E)$ representing the maximum of Young's modulus of the applied material distribution, proved to ensure both accurate results and numerical stability for all computed examples

² $\epsilon :=$ unit roundoff

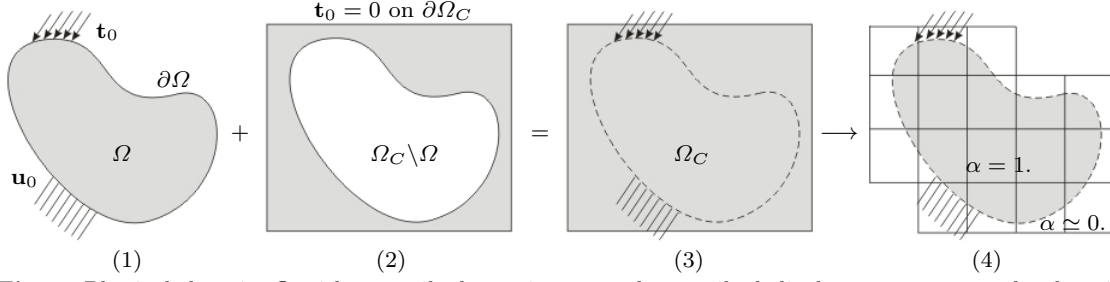


Fig. 4 Physical domain Ω with prescribed traction \mathbf{t}_0 and prescribed displacements \mathbf{u}_0 on the domain boundary $\partial\Omega$ (1), extended cell domain $\Omega_C \setminus \Omega$ with zero traction $\mathbf{t}_0 = 0$ on the cell domain surface $\partial\Omega_C$ (2), embedded domain with implicit domain support for Ω_C from prescribed displacement constraints on $\partial\Omega$ (3) and applied cell grid structure on Ω_C with location factor $\alpha = \{0, 1\}$ (4).

from linear analyses [15,16].

Since no body forces are applied in bone's domain $\mathbf{p}_V \equiv 0$ the first term of the right hand side of (7) vanishes. In general, the boundary of the cell domain $\partial\Omega_C$ is traction free due to the fact that traction forces are directly applied on the true domain boundary $\partial\Omega_t$. The same holds for the reaction forces \mathbf{t} along the boundary of prescribed displacements $\partial\Omega_u$. Thus the integrals for the known and unknown traction forces on $\partial\Omega_C$ have no contribution and are replaced by the last two integrals of (7).

Considering (8), the vanishing of the body forces and the assumptions for the boundary of the cell domain, (7) can be extended to the entire (much simpler) cell domain Ω_C . With $\partial\Omega = \{\partial\Omega_u \cup \partial\Omega_t\} \subset \Omega_C$ the formulation remains a consistent weak formulation for the linear elasticity problem on Ω_C .

$$\int_{\Omega_C} \delta \boldsymbol{\epsilon}^T \boldsymbol{\sigma}(\alpha) dv = \int_{\partial\Omega_u} \delta \mathbf{u}^T \mathbf{t} da + \int_{\partial\Omega_t} \delta \mathbf{u}^T \mathbf{t}_0 da$$

$$\mathbf{x} \in \partial\Omega_u \quad \Rightarrow \quad \mathbf{u} = \mathbf{u}_0 \quad (9)$$

3.2.2 Discretization

The Finite Cells are implemented as hexahedral elements according to the usual principles of the p-FEM. The unknown function \mathbf{u} is approximated in Ω_C with piecewise defined hierarchical polynomial functions $N_i(\xi, \eta, \zeta)$ of higher order specified in the standard hexahedral ($-1 \leq \xi, \eta, \zeta \leq 1$) (see e.g. [17])

$$\mathbf{u} = \sum_c \mathbf{N}^T(\xi, \eta, \zeta) \mathbf{R}_c \mathbf{U} \quad (10)$$

with $\mathbf{U}^T = [U_1 \dots U_N]$ representing the specified degrees of freedom in terms of cell displacements. It is important to realize that the vector \mathbf{U} of length N represents also the known degrees of freedom associated with the prescribed displacement on $\partial\Omega_u$. In this context, with each primal unknown on the boundary $\partial\Omega_u$, an associated traction is generated - on $\partial\Omega_t$ these tractions are known to be \mathbf{t}_0 , whereas on $\partial\Omega_t$ these tractions are unknowns to be determined by the solution of (9).

\mathbf{R}_c represents the topological mapping from cell to system level. The strain tensor $\boldsymbol{\epsilon}$ in (9) is approximated with the linear strain operator $\mathbf{B}(\xi, \eta, \zeta)$ that follows from the differentiation of the quantities of (10) with respect to the global coordinates (x_1, x_2, x_3) , applying the chain rule.

According to the method of Galerkin, the derivatives of (10) with respect to the quantities U_i ($i = 1, \dots, N$), are chosen as the variation of the introduced variables. Since only \mathbf{U} in (10) depends on the quantities U_i its i^{th} variation results in the unit vector \mathbf{e}_i ,

$$\delta \mathbf{u}^T = \delta(\mathbf{U}^T \mathbf{R}_c^T \mathbf{N})$$

$$= \frac{\partial \mathbf{U}^T}{\partial U_i} \mathbf{R}_c^T \mathbf{N} = \mathbf{e}_i^T \mathbf{R}_c^T \mathbf{N} \quad (11)$$

$$\delta \boldsymbol{\epsilon}^T = \delta(\mathbf{U}^T \mathbf{R}_c^T \mathbf{B})$$

$$= \frac{\partial \mathbf{U}^T}{\partial U_i} \mathbf{R}_c^T \mathbf{B} = \mathbf{e}_i^T \mathbf{R}_c^T \mathbf{B} \quad (12)$$

resulting in a system of N linear equations:

$$[\mathbf{K}] \mathbf{U} = \mathbf{Q} \quad (13)$$

with \mathbf{K} being the stiffness matrix and \mathbf{Q} representing the vector of load and unknown reaction forces.

3.2.3 Numerical integration on cell level

The integrals of (9) are evaluated on the cell level applying a numerical integration scheme. Various schemes were tested to reduce the numerical effort and to confine the integration error. In [10] a sub-cell integration scheme was proposed that decomposes the cell domain into a set of smaller integration units of arbitrary size applying standard Gauss quadrature with $(p + 1)^3$ quadrature points in each coordinate direction. This way the number of quadrature points can be densified locally, according to the structural needs of the geometric or physical configuration.

For homogeneous material properties the sub-cell scheme can be restricted to boundary cells to capture the true boundary of the physical domain Ω , whereas cells that are completely inside the domain are treated as standard p-elements. For this approach a tree-based decomposition strategy of the cell domain is favorably applied (Fig. 5). In the case of heterogeneous material properties as existing for the voxel model of a bone, a regular subdivision of each cell is applied to make allowance for the voxel-wise changing material properties. Yang et al. [12] developed an integration scheme for the inhomogeneous, isotropic case that pre-computes and stores the sub-cell matrices for a single Finite Cell independent of the Lamé constants λ and ν . During the assembly step of the system equations each cell stiffness is composed by scaling the pre-computed sub-cell matrices with the Lamé constants and summation over all sub-cells.

The cell stiffness matrix $[\mathbf{K}_c]$ is given by the integral

$$[\mathbf{K}_c] = \sum_{sc} \left\{ \int_{z_1} \int_{z_2} \int_{z_3} \hat{\mathbf{B}}_c^T [\mathbf{C}(\alpha)] \hat{\mathbf{B}}_c \det(\mathbf{J}_c) \det(\hat{\mathbf{J}}_{sc}) dz_1 dz_2 dz_3 \right\} \quad (14)$$

with \mathbf{J}_c and $\hat{\mathbf{J}}_{sc}$ representing the Jacobian of the Finite Cell and its sub-cells (index $\{.\}_{sc}$), respectively. The strain interpolation matrix $\hat{\mathbf{B}}_c$ is evaluated for each sub-cell in consideration of the mapping of the normalized coordinates (z_1, z_2, z_3) of a locally defined Cartesian coordinate system located in the sub-cell center to the normalized coordinate system of the

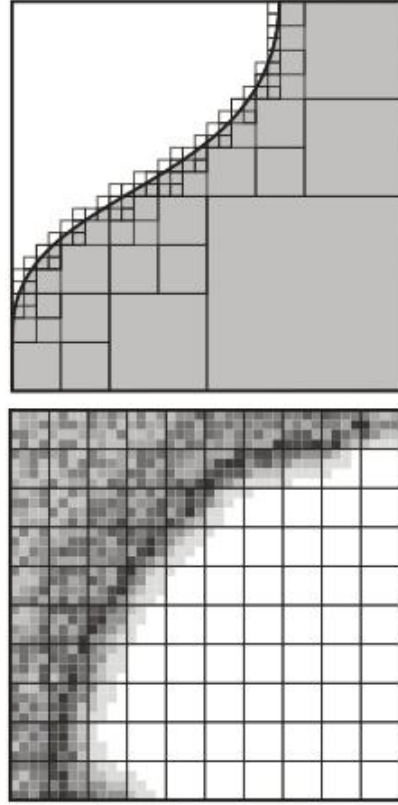


Fig. 5 Octree-based cell decomposition into sub-cells for boundary cells of homogeneous material (top) and uniform subdivision of a voxel-based material distribution as applied for CT-based bone models (bottom).

Finite Cell.

$$\hat{\mathbf{B}}_c = \mathbf{B}_c(\xi(z_1), \eta(z_2), \zeta(z_3)) \quad (15)$$

Since $[\mathbf{C}_\alpha]$ in (14) is a function of the location vector \mathbf{x} , the accuracy of the integral over the true physical domain is dominated by the density distribution of the integration points of each cell. For a heterogeneous voxel model as shown in Fig. 5 the true boundary is identified implicitly by the highly discontinuous development of the voxel values. The material function for the cells is evaluated at each integration point.

The evaluation of the load integral of the right hand-side of (9) follows in analogy to the integration of the stiffness matrix.

The integrals in (14) are evaluated numerically with Gauss quadrature. Due to the sub-cell approach and the use of an undistorted cell grid, only a small number of quadrature points per sub-cell is necessary to accurately compute the governing integrals. The number of sub-cells per finite cell was chosen such

³ p : polynomial degree

that each sub-cell covers 2^3 voxels. It turned out that 2^3 quadrature points per sub-cell are sufficient for an accurate computation of the integrals at a polynomial order of $p = 4$.

3.2.4 Boundary conditions

Boundary conditions are of special importance in the formulation of the FCM since they do not necessarily follow the standard approach that is applied for classical finite elements. For prescribed surface traction often a locally confined surface mesh is required to capture the true loaded surface area. The prescribed primal variables are weakly satisfied in the following by a Nitsche formulation of (9).

Neumann boundary conditions For a physical boundary $\partial\Omega$ coinciding with the Finite Cell boundary $\partial\Omega_C$, a standard approach is applied by integration over the cell boundary. Boundaries $\partial\Omega$ that do not coincide with the cell surface have to be treated differently and require additional effort. A strategy to resolve this problem was proposed in [10], an approach that is based on a locally bounded surface mesh to approximate the true boundary in the area of loading and to allow for accurate numerical integration.

In the present case the loaded surface on bone's head coincides with the bone surface on an inclined cutting plane through the femur head. For this approach the few relevant top cells were chosen to coincide on the top face with the cutting plane, resulting in marginally distorted geometries (Fig. 10). This special case allows a much simpler integration approach over the voxelized surface identifying the true loaded area in $\int_{\partial\Omega_t} \delta \mathbf{u} \mathbf{t}_0 da$ by the location factor $\alpha(\mathbf{x})$. The prescribed traction force \mathbf{t}_0 is defined on $\partial\Omega_C$ for $\alpha > \epsilon$ and is set to zero otherwise.

Dirichlet boundary conditions For the bone analysis, described in the following chapters, only homogeneous Dirichlet boundary conditions are of importance since the modelled femur bone is fully clamped at its distal face. Nevertheless the following treatment of the boundary conditions allows for other configurations, too.

In the classical FEM it is a common approach to satisfy the prescribed values for $\mathbf{u}(\mathbf{x})$

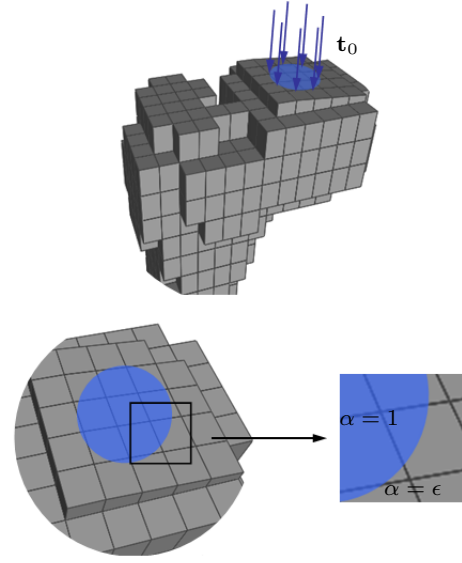


Fig. 6 Loaded area on inclined top cell surfaces. Numerical integration is performed over the cell surface and contributes to the load term for $\alpha > \epsilon$.

pointwise by setting $\mathbf{u} = \mathbf{u}_0 \forall \mathbf{x} \in \partial\Omega_u$ (Eq.(7)). Weak equivalent approaches are the penalty method [18,19] and the Lagrange multiplier method [20,19]. Both methods are applicable only in the case when the boundary of the domain coincides with the boundary of elements. Yet they fail, if the boundary passes through the interior of elements like in interface problems or for fictitious domain methods.

As an alternative to the aforementioned strategies to ensure arbitrary constraints, the method of Nitsche [21,22] is a consistent and stable formulation satisfying boundary conditions in the mean, thus conforming to the weak formulation of the FEM/FCM. Nitsche's method can be directly derived from the governing equations of the method of weighted residuals serving as a basis formulation for the extended principle of virtual displacements (section 3.2.1), augmented by weighting terms. Considering the additional terms of the Nitsche method, equation (9) is replaced by the following extended formulation which is consistent with the original problem and satisfies

$$W_\sigma(\mathbf{u}, \delta \mathbf{u}) = W_f(\delta \mathbf{u}) \quad \text{with} \quad (16)$$

$$\begin{aligned}
 W_\sigma(\mathbf{u}, \delta\mathbf{u}) &= \int_{\Omega_C} \delta\epsilon^T \boldsymbol{\sigma}(\alpha) dv \\
 &- \int_{\partial\Omega_u} \delta(\boldsymbol{\sigma} \mathbf{n})^T \mathbf{u} da - \int_{\partial\Omega_u} \delta\mathbf{u}^T (\boldsymbol{\sigma} \mathbf{n}) da \\
 &+ \beta \int_{\partial\Omega_u} \delta\mathbf{u}^T \mathbf{u} da \quad (17)
 \end{aligned}$$

$$\begin{aligned}
 W_f(\delta\mathbf{u}) &= \int_{\partial\Omega_t} \delta\mathbf{u}^T \mathbf{t}_0 da \\
 &+ \int_{\partial\Omega_u} \delta\mathbf{t}^T \mathbf{u}_0 da + \beta \int_{\partial\Omega_u} \delta\mathbf{u}^T \mathbf{u}_0 da \quad (18)
 \end{aligned}$$

with $\boldsymbol{\sigma} \mathbf{n} = \mathbf{t}$, \mathbf{n} is the normal vector to the boundary $\partial\Omega_u$ and β a stabilizing factor. The origin of the three additional terms in (17) and the additional term in (18) of the Nitsche extension is as follows: The second term in (17) and the second term in (18) result from the weakly satisfied weighted residual for the prescribed displacements that are satisfied pointwise in the classical formulation (7) and (9), respectively. The weighting function is chosen to ensure consistency in the physical dimension in (16).

$$\mathbf{u}_0 - \mathbf{u} = \mathbf{0} \quad \text{for } \mathbf{x} \in \partial\Omega_u$$

is replaced by

$$\int_{\partial\Omega_u} \delta\mathbf{t}^T \mathbf{u}_0 da - \int_{\partial\Omega_u} \delta\mathbf{t}^T \mathbf{u} da = \mathbf{0} \quad (19)$$

The third term in (17) corresponds to the integral term of unknown stresses (reaction forces) \mathbf{t} on $\partial\Omega_u$ of the extended formulation in (9) and ensures symmetry for the resulting matrices of the algebraic formulation. The last term in (17) and (18) correspond to classical penalty terms but with a different choice for the value of β . These terms ensure coercivity of the bilinear form (17) thus retaining positive definiteness for the resulting stiffness matrix. Nitsche proved in [22] optimal convergence to the exact solution in the H^1 - and L^2 -norm for a proper choice of β that can be found in dependence of the characteristic length h of the FE discretization and a large enough constant γ with $\beta = (\gamma/h)$.

With the right choice of β the weak form (17) results in a symmetric, positive definite

problem that ensures convergence under the assumption that

$$\|([\mathbf{C}]\delta\epsilon \mathbf{n})\|_{L_2(\partial\Omega)}^2 \leq C_N \|(\delta\epsilon^T [\mathbf{C}(\alpha)])\|_{L_2(\Omega_C)}^2 \quad (20)$$

holds for all $\delta\epsilon$ of the interpolation space and $\beta > 2C_N^2$ [23,21]. As a reliable estimate for C_N^2 Griebel and Schweitzer propose the largest eigenvalue λ_{max} of a generalized eigenvalue problem, based on (20) [23,24,21]. A detailed survey of Nitsche's method including the right choice for the weight factor β is beyond the scope of this paper and can be found in [24,23,21]. For the bone analysis in the course of this contribution a reliable value for β was found by experimental approximation to a stable configuration. For the applied cell structure, polynomial degree and material properties a value of $5 \cdot 10^4$ was chosen.

3.2.5 Verification of the FCM for an inhomogeneous isotropic material – Unit cube model

The following simplified numerical experiment is used to demonstrate the convergence behavior of the FCM for a unit cube with inhomogeneous material properties (Fig.7). It particularly reveals the modelling error for a continuous material distribution due to a voxel representation from qCT-data. Various levels of granularity were tested in terms of different voxel resolutions for the inhomogeneous material distribution and with regard to the number of integration points applied for Gauss quadrature. The summary of results is compared to the p-FEM approach used in subsection 3.1. The cube domain is given by:

$$\begin{aligned}
 \Omega &= \{(x, y, z) \mid -0.5 \leq x, y \leq 0.5, \\
 &0.0 \leq z \leq 1.0\} \quad (21)
 \end{aligned}$$

Symmetric boundary conditions are applied on the three faces $x = -0.5$, $y = -0.5$ and $z = 0.0$ and a normal unit traction is applied on face $y = 0.5$. The inhomogeneous material distribution is due to the elasticity modulus E and a constant Poisson ratio ν (Fig. 7).

$$\begin{aligned}
 E(x, y, z) &= (10 + x)^2(y + 10)(z + 1) \\
 \nu &= 0.3 \quad (22)
 \end{aligned}$$

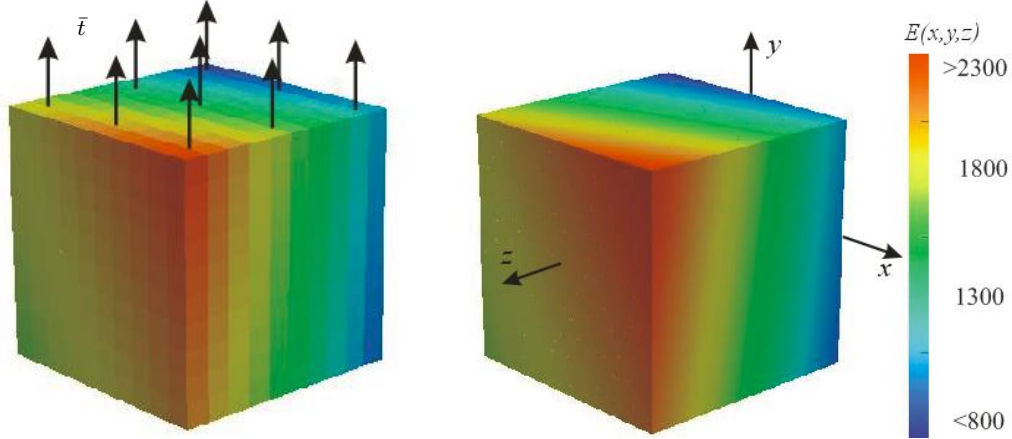


Fig. 7 Voxelized test cube with $10 \times 10 \times 10$ voxel (left) and continuous distribution of Young's modulus of the unit test cube (right)

A p-FEM solution of the continuous material model was analysed with $2 \times 2 \times 2$ hexahedral elements using $(p+1)^3$ Gaussian quadrature points for integration. For the FCM analysis the cube was also modeled by $2 \times 2 \times 2$ cells, resolving each voxel by one sub-cell applying $n=2$ quadrature points per sub-cell. In comparison, the cube was also analysed by the p-FEM applying a tetrahedral mesh generated automatically by a mesh generator as used for the bone analysis in section 3.1. Whereas the FCM integration scheme captures the inhomogeneity of the discrete material model by a highly resolved sub-cell scheme, the p-FEM approach applies a weighted point average method for each quadrature point, thus turning the discrete material distribution into a continuous function. A detailed overview about this approach is given in [9].

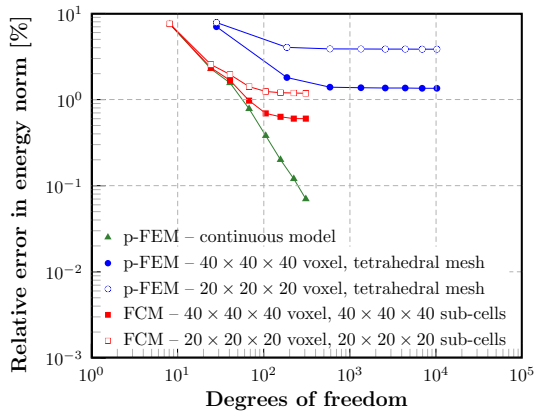


Fig. 8 Relative error in energy norm with regard to the continuous reference solution

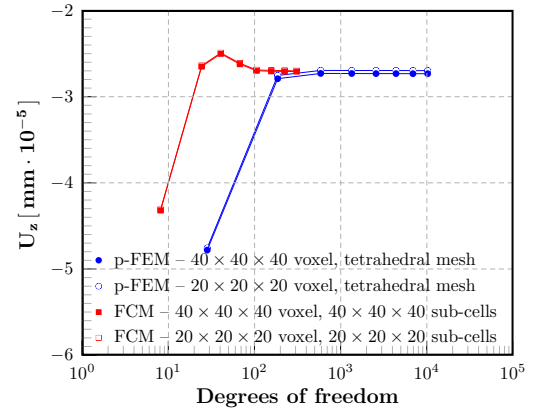


Fig. 9 Convergence behavior of the vertical displacement U_z

The graphs in Figure 8 present the relative error in energy norm (ordinate) against the total number of degrees of freedom for each model (abscissa). For the p-FEM reference solution of the continuous material model, an exponential convergence behavior is observable with increasing polynomial degree. The two proposed voxel-based analysis methods, the p-FEM and the FCM, show monotonic convergence to a fixed relative error if the material properties are given as discrete values in a table as in a CT-scan. The error norm of the plots was computed with regard to the continuous model as an independent reference solution. Thus the error plots provide a measure for the accuracy of the chosen granularity level rather than an estimate for the accuracy to the exact, unknown solution of a voxel resolved structure.

The numerical tests demonstrate that convergence is achieved for both methods at various voxel resolutions. With the $40 \times 40 \times 40$ voxel resolution for both methods a marginal modeling error is introduced as compared to continuous material properties. Figure 9 shows the convergence of the vertical displacement for a typical point of the test cube. Both resolutions show nearly identical results for each of the methods.

3.2.6 FCM model generation

The FCM model of the femur is derived from quantitative computer tomography scans (qCT) *without the need for segmentation*. Whereas the embedding domain is also considered for computation during the analysis, its material properties are chosen such that it has virtually no influence on the numerical results. Thus, the true structural boundary is only observed implicitly, not by an explicit boundary representation.

Cell model The solid model was meshed with 678 Finite Cells of constant size. For each cell the corresponding array of $(40 \times 40 \times 10)$ voxels/cell was assigned. Cells outside the physical domain were discarded to prevent ill-conditioned system equations, see Figure 10. The number of sub-cells that were used during the integration of the element matrices and vectors was adjusted to the number of voxels per cell. Before this discretization model was selected, several levels of granularity specified by various voxel allocations were chosen for an analysis to test for an optimal configuration, ranging from $(6 \times 6 \times 6)$, $(10 \times 10 \times 10)$, $(20 \times 20 \times 10)$ to the proposed configuration above. The coarsest model of $(40 \times 40 \times 10)$ voxels/cell turned out to be economical in terms of the computational effort providing a sufficient accuracy level at a polynomial degree of $p = 4$.

Boundary conditions The bone model was loaded with $1000N$ on top at an inclination angle of $\phi = 5.5^\circ$ in respect to the CT-scan, that corresponds to a force along the femur shaft as in the experiment. The model was fully constrained at the distal face. The loaded top cells and the constraint base cells deviate from the orthogonal grid scheme to account for the

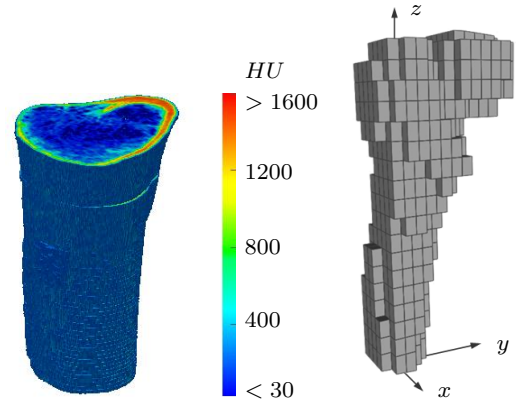


Fig. 10 Cross-section of the voxel model and HU distribution (left) and embedding Finite Cell model (right)

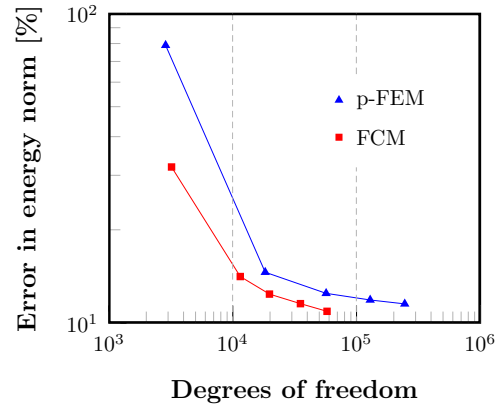


Fig. 11 FF4 p-FE and FCM convergence in energy norm

model rotation. A Cartesian coordinate system was specified at the bottom qCT-slice to uniquely identify the location and rotation of the bone, the applied load and the locations that were evaluated in the post-processing of the analysis.

Both, model generation and numerical analysis are implemented in the object-oriented C++ -framework *FELiNA++ (Finite Element Linear & Nonlinear Analyses)*. Verification results for the FCM implementation are provided by a p-refinement convergence study (see Figures 11, 12 and Table 2).

4 Numerical results and validation

The FCM and p-FEM predictions of the in-vitro test and their comparison to the experimental observations serve as a basis for the validation of the methods.

Table 3 Experimental, p-FE and p-FCM results – deviation from mean experimental results in percentage in brackets, displacements are reported in $\text{mm} \times 10^3$ and strains in μstrain .

Data		p-FEM (@p=5)	($\Delta\%$)	FCM (@p=4)	($\Delta\%$)	Exp.
U_y	Point	974	(7)	1063	(17)	912
	Face	1012	(11)	1089	(19)	
U_z	Point	566	(-25)	611	(-19)	753
	Face	531	(-30)	611	(-19)	
SG1	Point	-747	(-4)	-722	(-1)	-716
	Face	-753	(-5)	-655	(9)	
SG2	Point	-708	(-7)	-647	(2)	-660
	Face	-715	(-8)	-748	(-13)	
SG3	Point	-565	(8)	-586	(4)	-611
	Face	-586	(4)	-593	(3)	
SG4	Point	-808	(-3)	-847	(-8)	-782
	Face	-767	(2)	-860	(-10)	
SG5	Point	-634	(-6)	-714	(-19)	-600
	Face	-663	(-10)	-714	(-19)	
SG6	Point	-608	(-47)	-642	(-55)	-413
	Face	-600	(-45)	-648	(-57)	
SG7	Point	-470	(-8)	-511	(-17)	-437
	Face	-480	(-10)	-577	(-32)	
SG9	Point	-194	(-14)	-207	(-22)	-170
	Face	-273	(-61)	-212	(-25)	
SG10	Point	514	(16)	550	(24)	443
	Face	545	(23)	557	(26)	
SG12	Point	-383	(-3)	-502	(-35)	-371
	Face	-391	(-5)	-460	(-24)	
SG8	Point	-259	(-100)	-353	(-172)	-130
	Face	-308	(-137)	-407	(-213)	
SG11	Point	816	(221)	521	(105)	255
	Face	741	(191)	474	(86)	
SG13	Point	1045	(388)	762	(256)	214
	Face	832	(289)	741	(246)	

Table 2 FF4 FCM verification (678 Finite Cells)

P level	DOF	% Rel. error in energy norm	% Rel. error in U_z
1	3210	31.91	9.01
2	11532	14.12	0.55
3	19854	12.39	0.40
4	35325	11.54	0.27
5	57945	10.90	0.14

Strains and displacements in the FCM and p-FE models were extracted at the location of the SGs on the bone’s surface. We also computed ”surface data”, i.e. average data on the outer surface of the nearest element to the SG location. The experimental data was therefore normalized with respect to $1000N$ and average measured values were computed. In Table 3 we provide a summary of the experimental results together with the p-FE and FCM results.

Linear regression plots of the experiment results versus the p-FE and FCM predictions for displacements and strains are presented in Figure 13. A very good overall correlation between the experimental measurements and the numerical predictions is noticed with $R^2 > 0.96$ (Table 4). Though the point data extraction method provided a slightly better agreement between experimental and numerical results of both methods, the averaged surface data extraction method better simulates the actual data acquisition process. The slope of the linear regression for the FCM indicates a ”weaker” model that most likely results from the skyline surface of the embedding cells compared to the very smooth surface of the p-FE model. Another effect that contributes to a ”weaker” FCM model results from the oscillatory behavior of the strains in presence of a high disconti-

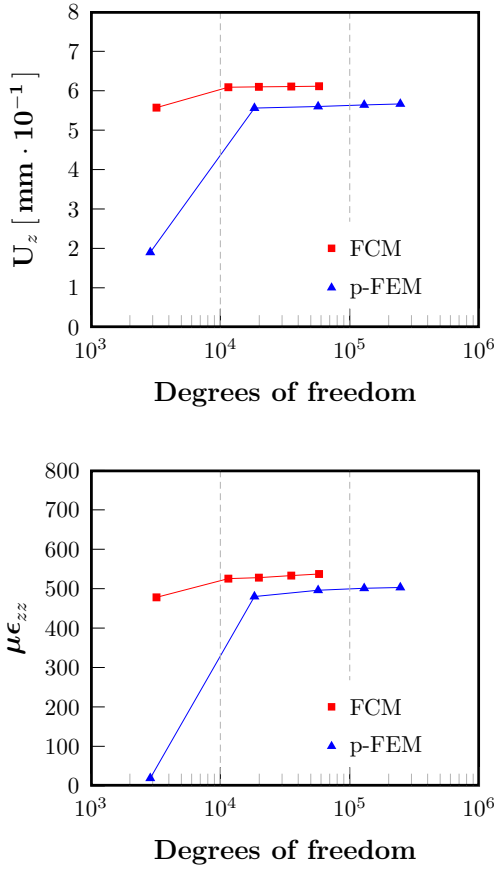


Fig. 12 FF4 p-FE and FCM convergence for different data of interest – pointwise displacement (top) and pointwise strain (bottom) for typical locations within Ω .

nity along the interface between bone surface and cell extension, an error that was systematically analysed in [25].

Table 4 Data correlation and slope of the linear regression

	Point values	Face average
R^2 (p-FEM)	0.990	0.987
R^2 (FCM)	0.975	0.962
Slope (p-FEM)	0.974	0.960
Slope (FCM)	0.916	0.882

5 Summary and conclusions

The non-standard FCM numerical simulation method for bone analysis was presented and

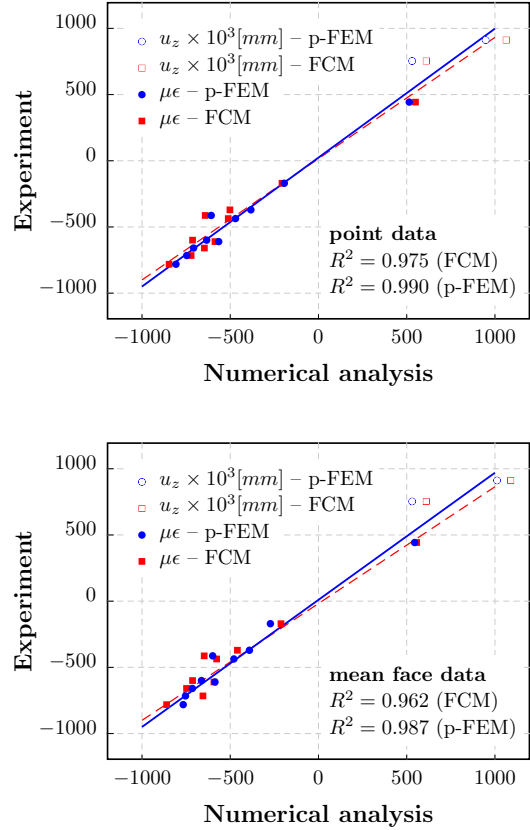


Fig. 13 Experimental results vs. p-FE and FCM predictions. Pointwise values (top) and element face average (bottom)

compared to a well documented and accurate p-FEM as well as to experimental observations on a fresh-frozen human femur for validation purposes. As the segmentation step is avoided by the FCM, one may apply the method directly on the qCT scans, and thereafter monitor the accuracy level by increasing the polynomial order and granulation of the underlying integration scheme.

The fundamentals and specifics of the newly developed FCM with particular emphasis on the simulation of bones from qCT data are derived and documented. The performance of the FCM as compared to the p-FEM for an inhomogeneous isotropic material is demonstrated by a benchmark test to prove the efficiency for bone simulation. A comparison of both methods with regard to the femur analysis includes a pointwise measure of principal strains on the bone surface, an averaged result over surface data for each position and displacement values

on the femur head. Both methods show a very good correlation with the measured experimental values. Even the critical parts on the femur head are of a highly satisfying quality and underline the reliability of both methods. The p-FEM analysis shows slightly better results due to a smoother surface model and a higher polynomial degree that was used in the analysis.

In this research we focused on the verification and validation of the FCM and the comparison with the p-version of the Finite Element Method. Both methods are very effective and reliable simulation schemes that provide a measure of high quality results in this field. With an extension to a pre-computation concept for the stiffness matrices, a research that is in preparation for publication, the FCM analysis in addition provides high update rates that allow user interactive exploration of the mechanical response of the femur for continuously changing loads. With such a numerical efficiency the FCM is ideally suited to be integrated into a computational-steering and visualization environment as presented in [12].

Acknowledgements We would like to thank Prof. Charles Milgrom from the Hadasah Hospital, Jerusalem for the femurs and his help with the CT-scans and experiments. The authors gratefully acknowledge the generous support of the Technische Universität München - Institute for Advanced Study and International Graduate School of Science and Engineering, funded by the German Excellence Initiative, which made this research possible.

References

1. E. Schileo, E. Dall'Ara, F. Taddei, A. Malandrino, T. Schotkamp, M. Viceconti, An accurate estimation of bone density improves the accuracy of subject-specific finite element models, *Journal of Biomechanics* 41 (2008) 2483–2491.
2. E. Schileo, F. Taddei, A. Malandrino, L. Cristofolini, M. Viceconti, Subject-specific finite element model scan accurately predict strain levels in long bones, *Journal of Biomechanics* 40 (2007) 2982–2989.
3. J. Keyak, Y. Falkinstein, Comparison of in situ and in vitro CT-scan-based finite element model predictions of proximal femoral fracture load, *J. Med. Eng. Phys.* 25 (2003) 781–787.
4. M. Viceconti, M. Davinelli, F. Taddei, A. Cappello, Automatic generation of accurate subject-specific bone finite element models to be used in clinical studies, *Journal of Biomechanics* 37(10) (2003) 1597–1605.
5. J. Keyak, M. Fourkas, J. Meagher, H. Skinner, Validation of an automated method of three-dimensional finite element modelling of bone, *Journal of Biomedical Engineering* 15(6) (1992) 505–509.
6. Z. Yosibash, N. Trabelsi, C. Milgrom, Reliable simulations of the human proximal femur by high-order finite element analysis validated by experimental observations, *Journal of Biomechanics* 40 (2007) 3688–3699.
7. Z. Yosibash, R. Padan, L. Joscowicz, C. Milgrom, A CT-based high-order finite element analysis of the human proximal femur compared to in-vitro experiments, *ASME J. Biomechanics Eng.* 129(3) (2007) 297–309.
8. F. Taddei, M. Pani, L. Zovatto, E. Tonti, M. Viceconti, A new meshless approach for subject-specific strain prediction in long bones: Evaluation of accuracy, *Clinical Biomechanics* 23(9) (2008) 1192–1199.
9. N. Trabelsi, Z. Yosibash, C. Milgrom, Validation of subject-specific automated p-FE analysis of the proximal femur, *Journal of Biomechanics* 42 (2009) 234–241.
10. A. Düster, J. Parvizian, Z. Yang, E. Rank, The finite cell method for three-dimensional problems of solid mechanics, *Computer Methods in Applied Mechanics and Engineering* 197 (2008) 3768–3782.
11. J. Parvizian, A. Düster, E. Rank, Finite cell method – h- and p-extension for embedded domain problems in solid mechanics, *Comput. Mech.* 41 (2007) 121–133.
12. Z. Yang, C. Dick, A. Düster, M. Ruess, R. Westermann, E. Rank, Finite cell method with fast integration - an efficient and accurate analysis method for CT/MRI derived models, in: *Proceedings of the ECCM 2010*, 2010.
13. J. Keyak, A. Koyamad, A. LeBlanc, Y. Lu, T. Lang, Reduction in proximal femoral strength due to long-duration spaceflight, *Bone* 44 (3) (1999) 449–453.
14. V. Galishnikova, P. Dunaiski, P. Pahl, *Geometrically nonlinear analysis*, Sun Press - Sun Media, Stellenbosch, 2009.
15. M. Ruess, E. Rank, From voxel-FEM to p-FEM-based analyses in bone mechanics, in: *Proceedings of the 2010 EMI Conference*, 2010.
16. M. Ruess, R. Mundani, R. Burgkart, A. Düster, E. Rank, R. Westermann, Computational steering for orthopaedics, in: *BIO Materialien*, Vol. 9, 2008.
17. B. Szabó, I. Babuška, *Finite Element Analysis*, John Wiley & Sons, New York, 1991.
18. I. Babuška, The finite element method with penalty, *Mathematics of Computation* 27(122) (1973) 221–228.
19. K.-J. Bathe, *Finite Elemente Methoden*, Springer Verlag, 2002.
20. I. Babuška, The finite element method with Lagrange multipliers, *Numerische Mathematik* 20 (1973) 179–192.
21. P. Hansbo, Nitsche's method for interface problems in computational mechanics, *GAMM Mitteilungen* 28/2 (2005) 183–206.

-
22. J. Nitsche, Über ein Variationsprinzip zur Lösung von Dirichlet-Problemen bei Verwendung von Teilräumen, die keinen Randbedingungen unterworfen sind, Abhandlung aus dem Mathematischen Seminar der Universität Hamburg 36 (1970) 9–15.
 23. M. Griebel, M. Schweitzer, A particle-partition of unity method. Part V: Boundary conditions, Springer-Verlag, Berlin, 2002.
 24. S. Fernández-Méndez, A. Huerta, Imposing essential boundary conditions in mesh-free methods, *Comput. Methods Appl. Mech. Engrg* 193 (2004) 1257–1275.
 25. D. Schillinger, S. Kollmannsberger, R. Mundani, E. Rank, The Finite Cell Method for Nonlinear Problems of Solid Mechanics, in: *Proc. of the World Conference on Computational Mechanics*, Sidney, 2010.